Energy Storage Materials 29 (2020) 113–120

Contents lists available at ScienceDirect

Energy Storage Materials

journal homepage: www.elsevier.com/locate/ensm

Reversible V^{3+}/V^{5+} double redox in lithium vanadium oxide cathode for zinc storage

Pan He [a], Mengyu Yan [a,b], Xiaobin Liao [a], Yanzhu Luo [c,**], Liqiang Mai [a,*], Ce-Wen Nan [a,d]

[a] State Key Laboratory of Advanced Technology for Materials Synthesis and Processing, Wuhan University of Technology, Wuhan, 430070, PR China
[b] Department of Materials Science and Engineering, University of Washington, Seattle, WA, 98195-2120, United States
[c] College of Science, Huazhong Agricultural University, Wuhan, 430070, PR China
[d] Department of Materials Science and Engineering, University of Tsinghua, Beijing, 100000, PR China

ARTICLE INFO

Keywords:
Double redox
LiV_3O_8
Zn ion batteries
Bi-electronic transfer

ABSTRACT

Zn ion batteries show great potential for large-scale energy storage owing to their low-cost, safe and environment-friendly features. There is an urgent need for cathode material with high-energy-density and long-service-life. Vanadium-based cathodes would be particularly desirable due to the bi-electronic transfer reaction ($V^{5+}/V^{4+}/V^{3+}$). Herein, we present a reversible V^{3+}/V^{5+} double redox in lithium vanadium oxide (LiV_3O_8) with the insertion of Zn^{2+} for ZIBs. In this way, six-electron transition in LiV_3O_8 was achieved with only 7.64% volumetric expansion, yielding the highest capacity of 557.5 mA h g^{-1}, and good cycling retention of 85% over 4000 cycles. The use of V^{3+}/V^{5+} double redox will open-up new opportunities for designing vanadium-rich cathodes for high-performance Zn ion battery.

1. Introduction

Renewable energy resources have gained the global spotlight owing to continuous environmental pollution and energy consumption, which greatly stimulates the development of scalable energy storage systems [1]. Among various storage options, lithium-ion batteries (LIBs) dominate the markets for decades because of their high energy densities [2]. However, the large-scale applications of LIBs are limited by the continuously increasing cost and potential safety hazard [3]. As an alternative, batteries based on low-cost and abundant Mg, Al, and Zn anodes have received increasing attention [4]. Especially, compared with magnesium ion batteries (MIBs) or aluminum ion batteries (AIBs), zinc ion batteries (ZIBs) show unique advantage due to their applicability to the aqueous electrolytes, which show higher ionic conductivities, better safety, and lower cost [5]. Whereas, the aqueous zinc systems suffer enduring challenges of cathode materials, such as limited capacity, low working voltage, and poor cycle life, which are caused by the cathode dissolution, and the side reactions of H_2/O_2 evolution [6].

In recent years, a series of materials with various structures were investigated as the cathodes for ZIBs, including manganese oxides [7], chalcogenides [8–10], Prussian blue analogous [11], Na superionic conductor (NASICONs) [12–14], and $ZnMn_2O_4$ spinels [15,16]. However, the capacities (<300 mA h g^{-1}) and/or the cycling life (<1000 cycles) were not satisfactory. Recently, substantial optimization strategies have been used to address the issues above. The structure water showed a lubricating effect during Zn^{2+} insertion in bilayer $V_2O_5{\cdot}nH_2O$ cathode, which was demonstrated by Mai and Wang et al. [17,18]. By controlling the phase, various structures of manganese oxides (α, β, γ, δ, and ε-type MnO_2) were investigated as hosts for ZIBs in the nearly neutral electrolyte, which showed improved cycling stability compared with traditional alkaline zinc-manganese battery [19–27]. In addition, the cycling life was further improved by using Mn^{2+}-addictive electrolyte, which could balance the Mn^{2+} between the electrode and the electrolyte. However, due to the sluggish Zn^{2+}-intercalation dynamics in the MnO_2 structure, limited Zn^{2+}-intercalation can be realized at the high rate in the MnO_2 electrode material.[21] Compared with MnO_2, vanadium-based materials show superior kinetics of Zn^{2+} and higher theoretical capacity owing to the multi-valence of vanadium [28,29]. Furthermore, by stabilizing/enlarging the diffusion channel, the $Na_{0.33}V_2O_5$ nanowires, bilayer $Zn_{0.25}V_2O_5{\cdot}nH_2O$, and $Ca_{0.25}V_2O_5{\cdot}nH_2O$ were designed, which showed excellent cycling stability (≥1000 cycles) [30–32]. This consideration, designing suitable vanadium-rich cathodes with faster insertion kinetics for Zn^{2+} is promising for constructing high capacity and long-life ZIBs.

* Corresponding author.
** Corresponding author.
E-mail addresses: luoyanzhu@mail.hzau.edu.cn (Y. Luo), mlq518@whut.edu.cn (L. Mai).

https://doi.org/10.1016/j.ensm.2020.04.005
Received 1 February 2020; Received in revised form 16 March 2020; Accepted 7 April 2020
Available online 14 April 2020

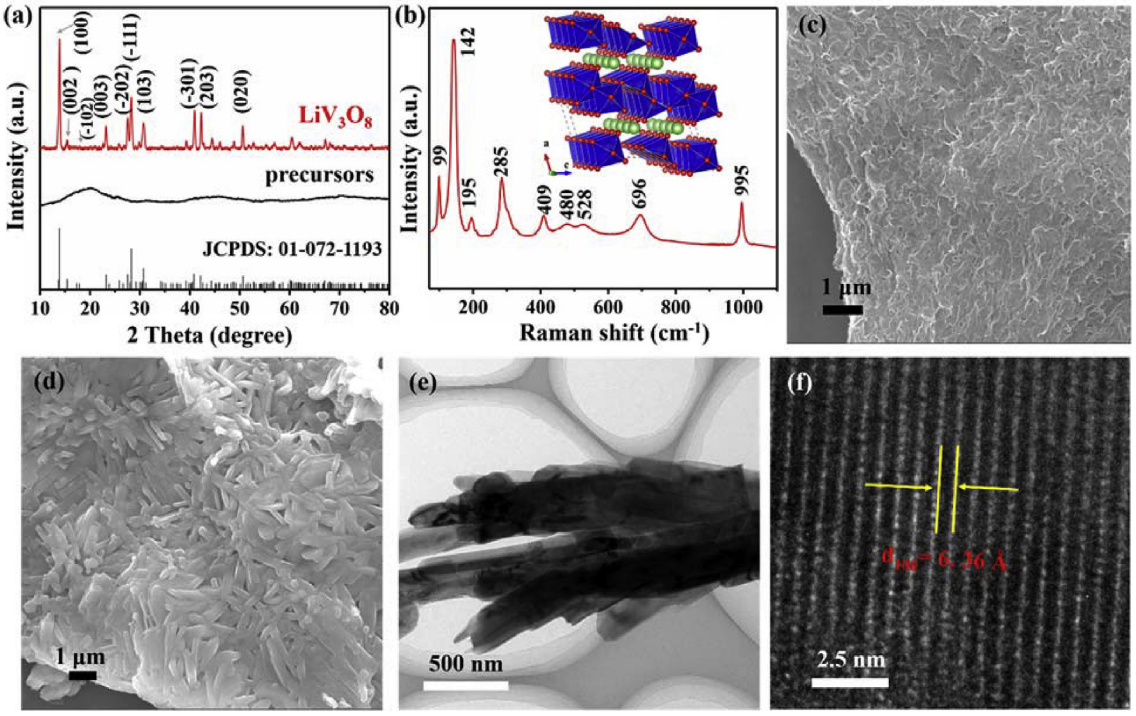

Fig. 1. The crystal structure and morphology characterizations of LiV_3O_8. (a) XRD patterns of the precursors (black line) and LiV_3O_8 (red line). (b) Raman spectrum in the range of 60–1100 cm^{-1}, the inset displays the crystal structure. SEM images of the precursors (c) and LiV_3O_8 (d). TEM image (e) and HRTEM image (f) of selected LiV_3O_8 nanorod. (For interpretation of the references to color in this figure legend, the reader is referred to the Web version of this article.)

The layered LiV_3O_8 shows feasibility for hosting excess guest ions [33]. Firstly, the high oxidation state (V^{5+}) of vanadium holds the capability for a bi-electronic transfer reaction ($V^{5+}/V^{4+}/V^{3+}$), yielding an extremely high theoretical capacity of ~560 mA h g^{-1} based on the reaction of V^{5+} converting to V^{3+}. Secondly, there are plenty of vacant sites in the layered structure of LiV_3O_8, which provide sufficient intercalation sites for the guest ions. The literature-reported results show the theoretical capacity of LiV_3O_8 for LIBs is ~280 mA h g^{-1} according to three Li ions intercalation per formula unit [34]. Compared with Li^+/Na^+ intercalation, the divalent Zn^{2+} intercalation provides the possibility to double the electron transitions under the same intercalation quantities, thereby doubling capacities. In addition, the approximate ionic radii of Zn^{2+} (0.74 Å) and Li^+ (0.76 Å) show the potential for three Zn ions intercalation per formula unit, which further support our hypothesis. The Zn^{2+} storage in LiV_3O_8 particles was reported in previous work by Kim et al. [35]. However, they only investigated the insertion of 1.5 mol Zn^{2+} into LiV_3O_8 with reversible V^{4+}/V^{5+} redox in the voltage of 0.6–1.2 V, delivering the discharge capacity of 256 mA h g^{-1}, which is far below the assuming theoretical capacity as discussed above (~560 mA h g^{-1}). So, it's urgent to realize the fully zinc insertion in the LiV_3O_8 (3 mol Zn^{2+} insertion) to achieve higher energy density. More importantly, the storage mechanism and reaction kinetics are expected to be more complex under this situation. As a result, the fully understanding of the storage mechanism, structural evolution of the electrode material, and the changes of reaction kinetics based on this bi-electronic transfer reaction mechanism is interesting and necessary.

Herein, we demonstrated a new stepwise insertion of Zn^{2+} in LiV_3O_8 cathode with reversible V^{3+}/V^{5+} double redox mechanisms. Six-electron transition in LiV_3O_8 was achieved with only 7.64% volumetric expansion, yielding the highest capacity of 557.5 mA h g^{-1}, and good cycling retention of 85% over 4000 cycles. The use of the V^{3+}/V^{5+} double redox will open-up new opportunities for designing vanadium-rich cathodes for high-performance Zn ion battery.

2. Results and discussion

2.1. Characterization of LiV_3O_8 nanorods

A facile and scalable liquid stirring followed by solid annealing method was adopted to prepare LiV_3O_8 nanorods (*Supplementary Information*). The precursor shows a non-crystalline structure as detected by X-ray diffraction (XRD) (Fig. 1a). After annealed at 450 °C for 2 h, the crystalline LiV_3O_8 is formed with characteristic diffraction peaks, which are consistent with monoclinic LiV_3O_8 with P21/m space group (JCPDS: 01-072-1193, a = 6.68 Å, b = 3.60 Å, c = 12.03 Å). The LiV_3O_8 is composed of VO_6 octahedrons and edge-sharing VO_5 tetragonal, forming V_3O_8 layers structure with lithium ions pillars (inset in Fig. 1b). The Raman spectrum shows nine characteristic peaks in the range of 60–1100 cm^{-1} (Fig. 1b), which qualitatively reflect the vibrations of V–O bonds along coordinate axes based on the atomic displacements in LiV_3O_8 unit cell [36]. Typically, the low-wavenumber peaks (99, 142, and 195 cm^{-1}) usually derive from the relative motions of the chain translation, which are associated with the layered structure. The peaks, in the medium/high wavenumber region (285, 409, 480, 528, and 696 cm^{-1}), reflect the stretching/bending of V–O, V–O–V, and O–V–O bonds in the internal modes. Specifically, the peak at 995 cm^{-1} is assigned to the shortest V^{5+}=O bonds oriented along the c-axis [37]. The field emission scanning electron microscopic (FESEM) image of the precursor shows a uniform wrinkle sheet structure (Fig. 1c). After the thermal treatment, a block with abundant cross-linking is obtained, which consists of nanorods with several micrometers in length, 200–500 nm in width (Fig. 1d). Transmission electron microscopic (TEM) image displays solid nanorods structure with smooth surfaces (Fig. 1e). The high-resolution TEM (HRTEM) image (Fig. 1f, Fig. S1a) shows a spacing of 6.36 Å, corresponding to the d-spacing of the (100) planes of LiV_3O_8 nanorods. The selected area electron diffraction (SAED) pattern demonstrates the single crystalline nature of the LiV_3O_8 nanorods (Fig. S1b).

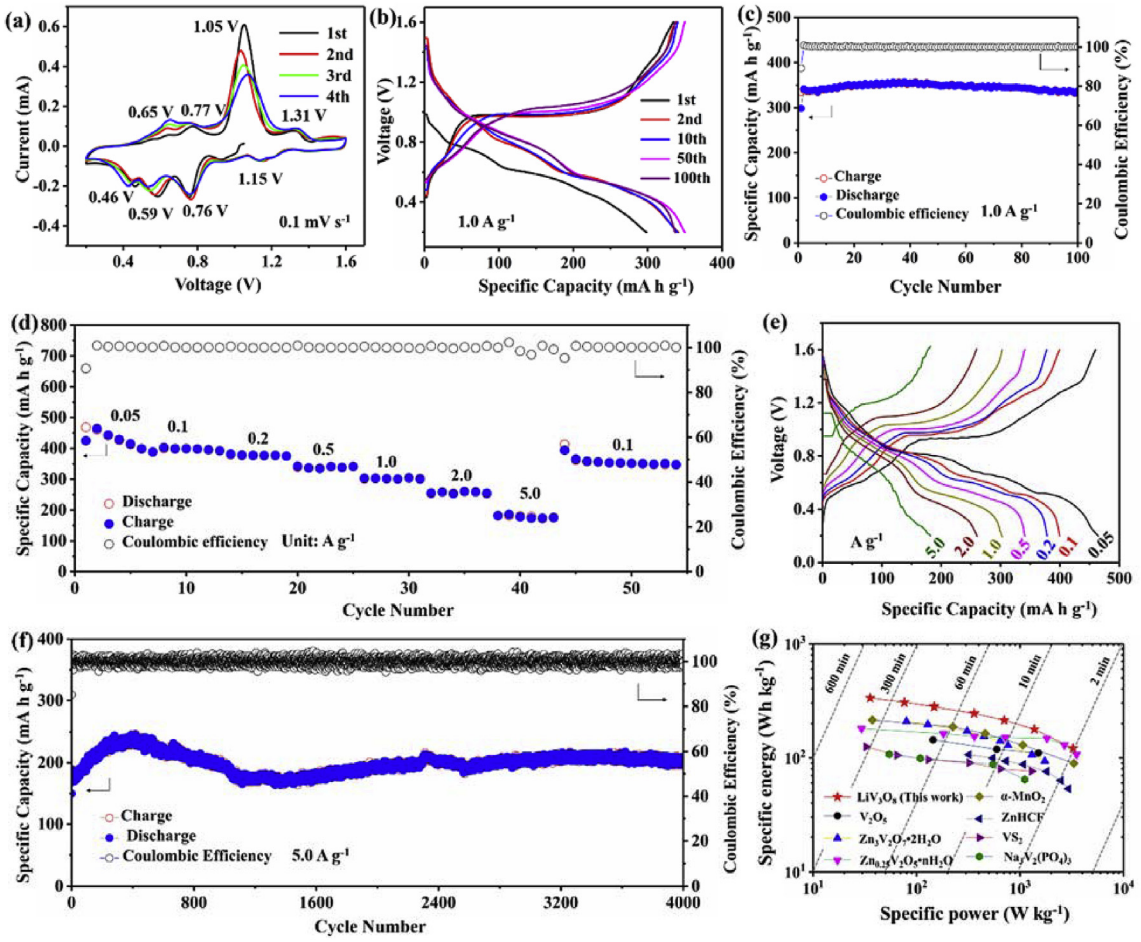

Fig. 2. Electrochemical performances of the Zn//LiV_3O_8 full cell. (a) The cyclic voltammetry curves of initial four cycles at the scan rates of 0.1 mV s^{-1}. (b) Galvanostatic charge and discharge profiles at the current density of 1.0 A g^{-1}. (c) Galvanostatic cycling at 1.0 A g^{-1}. (d) Rate capability at various rates and the Coulombic efficiencies, (e) and corresponding galvanostatic charge and discharge profiles. (f) Extended cycling performance and the corresponding coulombic efficiency at 5.0 A g^{-1}. (g) Comparison of the Ragone plot with different materials for ZIBs.

2.2. *Electrochemistry performances of Zn//LiV_3O_8 cells*

The electrochemical performances of LiV_3O_8 are investigated by assembling coin cell with Zn foil anode and 3 M $Zn(CF_3SO_3)_2$ electrolyte. The open-circuit voltages of these systems are in the range of 0.95–1.25 V, and gradually stabilize at about 1.30 V after resting for 3 h. Also, the systems show excellent stability with negligible self-discharge after 432 h (Fig. S2). The initial four cyclic voltammetry (CV) profiles (Fig. 2a) show four pairs of reduction/oxidation peaks, located at 0.46/0.65, 0.59/0.77, 0.76/1.05, and 1.15/1.31 V, respectively, indicating a multistep reaction mechanism. The Zn//LiV_3O_8 battery shows an extremely high capacity of ~450 mA h g^{-1} at the current density of 0.1 A g^{-1} in the initial several cycles and stabilizes at 350.2 mA h g^{-1} after 60 cycles (Fig. S3). Notably, the capacity of LiV_3O_8 nanorods is much higher than the previous result [35], which is attributed to various optimizations: (1) the extended operating voltage range ensures the fully reaction of the cathode; (2) the optimized electrolyte exhibits faster kinetics and better reversibility of Zn deposition/dissolution [16]; (3) the one-dimension nanorods exhibit better adhesion onto a current collector, unique structural stability for ion storage [2]. The galvanostatic charge/discharge profiles at 1.0 A g^{-1} are shown in Fig. 2b. An initial discharge capacity of 298.4 mA h g^{-1} is achieved with the Coulombic efficiency of ~89.2%. In the subsequent 2^{nd} - 100^{th} cycles, the battery delivers a capacity of ~345 mA h g^{-1}, with an average operating voltage of ~0.72 V. In addition, the voltage profiles are nearly overlapped, suggesting slight structural changes, which indicates a reversible process. Impressively, an extremely high capacity of 337.1 mA h g^{-1} is maintained after 100 cycles, with a capacity retention of 94.3% (against the highest capacity of 357.3 mA h g^{-1}) (Fig. 2c). The LiV_3O_8 cathodes also show outstanding rate capability (Fig. 2d). They exhibit a very high capacity of 464.2 mA h g^{-1} at 0.05 A g^{-1}. Even after the current density increasing to a hundred times (5.0 A g^{-1}), a capacity of 182 mA h g^{-1} is still achieved. Meanwhile, after cycled at various current rates, the capacity can recover to 394.5 mA h g^{-1} (85% capacity retention) as the current density abruptly recovers from 5.0 to 0.1 A g^{-1}, indicating high reversibility of the redox reactions and excellent crystal structure stability. Furthermore, the sloping discharge profiles at 0.05 A g^{-1} can be divided into four stages, thus 1.6–0.87, 0.87–0.70, 0.70–0.55, and 0.55–0.2 V, respectively, indicating a complex reaction mechanism (Fig. 2e). Interestingly, the plateaus below 0.65 V in discharge curves can hardly be distinguished at high rates, which will be discussed in the part of storage mechanism in detail. When cycled at a high rate of 5.0 A g^{-1}, an average capacity of ~200 mA h g^{-1} is achieved over 4000 cycles, with capacity retention of 85% (Fig. 2f). It's worth noting that the increased specific capacity of LiV_3O_8 cathode in the initial 400 cycles is attributed to the gradually activating process and electrolyte penetrating in the active material, which is commonly observed in vanadium-based electrode materials [38]. In summary, the LiV_3O_8 cathodes exhibit both impressive high energy density (~400 W h kg^{-1}) and outstanding power density (~4200 W kg^{-1}), which demonstrates a superior electrochemical performance among the previous reported

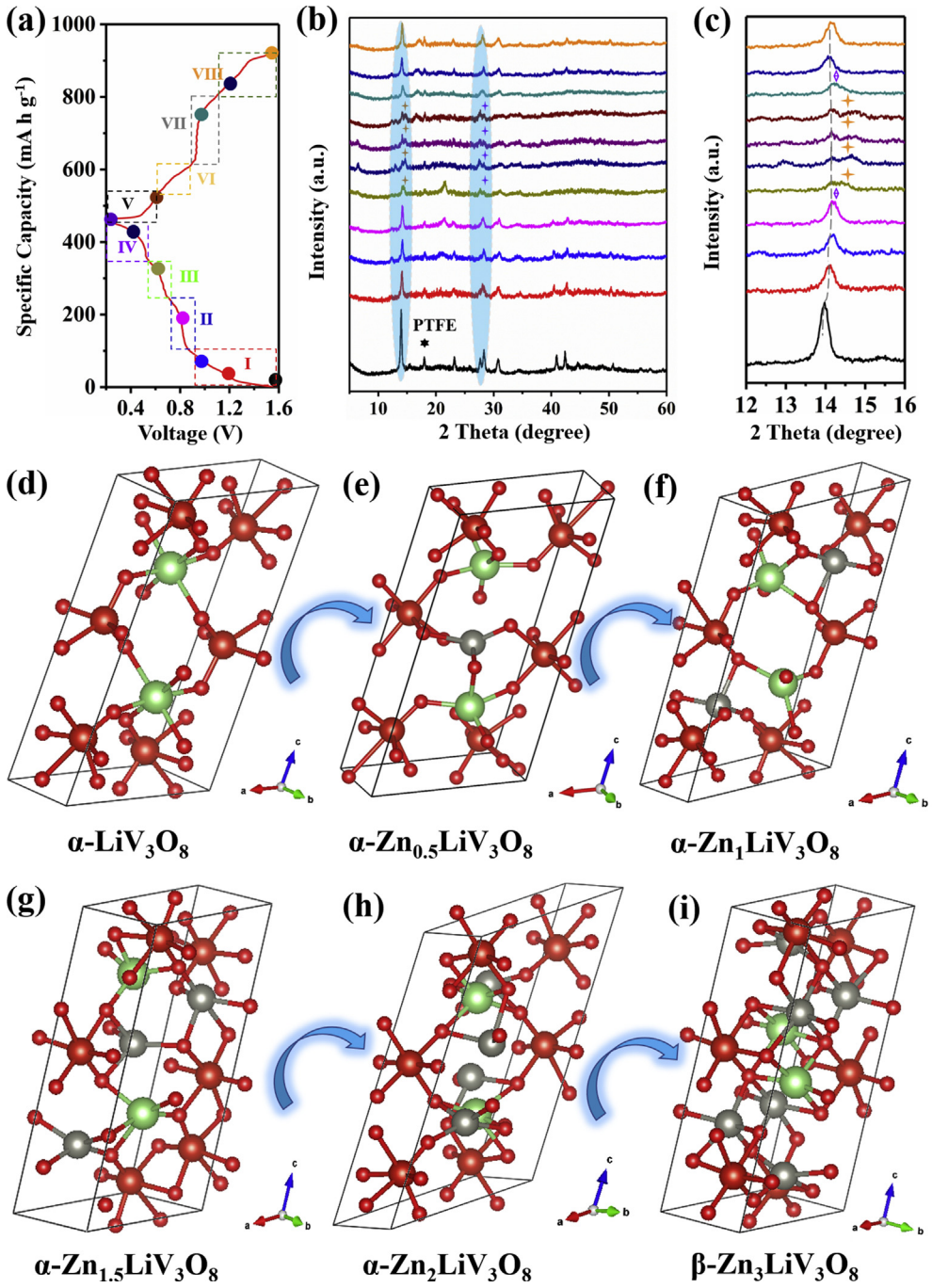

Fig. 3. (a) Galvanostatic charge and discharge profiles during the third cycle at 0.1 A g^{-1}, (b–c) *ex situ* XRD patterns, (d–i) structure/phase evolutions models of LiV_3O_8 during Zn^{2+} intercalation by DFT calculations.

works (Fig. 2g) [9,11,14,21,32,39,40].

2.3. Energy storage mechanism and structural evolution

The Zn^{2+} insertion mechanism in LiV_3O_8 was investigated by *ex situ* XRD during the third cycle at 0.1 A g^{-1} (Fig. 3a). The diffraction peak at 18.1° is attributed to the poly(tetrafluoroethylene) (PTFE) binder, which does not change upon cycling. The reversible shifts, appearance, and disappearance of the diffraction peaks are attributed to the active material phases transformation during discharge/charge process. The characteristic diffraction peaks at 13.92°, 23.28°, and 28.36°, reflect to the (100), (003), and (−111) lattice planes, respectively. According to the discharge curve and *ex situ* XRD patterns, the Zn insertion process can be divided into four regions, as marked by the red (Step I), blue (Step II), green (Step III), and purple (Step IV) colored boxes (Fig. 3a). In the first discharge region (1.60–0.87 V), the diffraction peak of (100) plane reveals a slightly shift to the higher angle with the intercalation of ~0.5 Zn^{2+} per formula (Fig. 3c), and the corresponding discharge potential curve shows a gradual slope, which reveals that a solid-solution behavior predominates in this single-phase domain ($Zn_xLiV_3O_8$, $0 < x \leq 0.5$) [35]. In the subsequent discharge process (0.87–0.55 V), the (100) diffraction peak shifts from 13.92° to 14.41°, indicating the reduction of the respective (100) distance, which is closely related to strong electrostatic interaction between the (V_3O_8)-layers framework and the intercalated Zn^{2+}. A splitting diffraction peak of the (100) is accompanied with the shift, and the corresponding discharge potential curve shows two

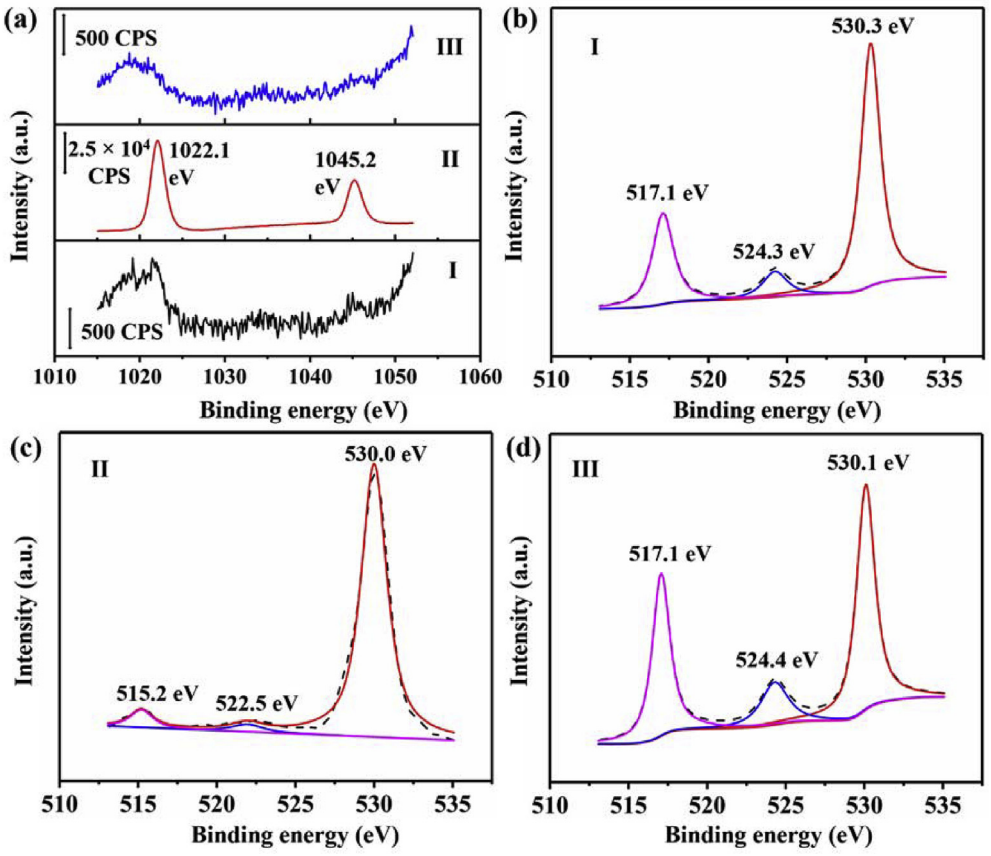

Fig. 4. X-ray photoelectron spectroscopic analysis of the electrodes. (a) Zn 2p region of the XPS spectra, Zn 2p component (2p3/2: 1022.1 eV). (b–d) V 2p region of the XPS spectra, (I) initial state, II (discharge to 0.2 V), III (recharge to 1.6 V).

consecutive discharge platforms, indicating that a successive two-phase transformation process may occur in this region ($Zn_xLiV_3O_8$, $0.5 < x < 2$). In the last discharge process (Region IV, from 0.55 to 0.20 V), there are two diffractions at 14.66° (denoted as (100)*) and 28.61° (denoted as (−111)*) splitting from their original positions and gradually increase in intensity, indicating a phase transition between the initial α-$LiZn_xV_3O_8$ ($x < 2$) and the newly formed phase of β-$LiZn_yV_3O_8$ ($2 \leq y \leq 3$). Interestingly, this phase transition would not generate at high discharge current densities ($\geq$ 0.5 A g^{-1}) with the intercalation of Zn^{2+} content below 2.0 Zn^{2+} per formula. The reverse evolutions show some differences in the following charge process. In the initial charge region (step V), the diffraction of (100) lattice plane shifts to lower position along with the disappearance of the diffraction of (100)* lattice plane, indicating a solid-solution behavior accompanying the β-$LiZn_yV_3O_8$ phase transform to α-$LiZn_xV_3O_8$ caused by the de-intercalation of Zn^{2+}. In the following process, two solid-solution regimes (step VI and step VIII) separated by a two-phase process (step VII) are observed, and the diffraction of (100) lattice plane return to the origin position, indicating a highly reversible process of Zn storage in LiV_3O_8 host. These unique discharge/charge reaction mechanisms are related to the Zn^{2+}-content during the intercalation/de-intercalation process.

To get further insights into the Zn storage mechanism, density functional theory (DFT) simulations are performed to investigate the structural evolutions of LiV_3O_8 during the Zn^{2+}-intercalation process. The initial lattice parameters calculated by DFT shows a similar result to the data obtained from XRD, and corresponding detail information is listed in Table S1. The structure/phase evolutions and Zn^{2+} insertion sites in LiV_3O_8 with different energies are predicted by DFT simulations based on the lowest energy solution (Figs. S4a–b, Table S2). In the initial stage of Zn intercalation, there is a 5.90% increase in unit cell volume from LiV_3O_8 to $Zn_1LiV_3O_8$ (Fig. 3d–f), which is attributed to the single-phase reaction (from LiV_3O_8 to $Zn_{0.5}LiV_3O_8$) and the two-phase reaction (from $Zn_{0.5}LiV_3O_8$ to $Zn_1LiV_3O_8$) during this process. With the increase of Zn^{2+} content, the unit cell volume shows 0.33% decrease from $Zn_1LiV_3O_8$ to $Zn_{1.5}LiV_3O_8$ (Fig. 3g), which relates to the closer (V_3O_8)-layers caused by the Zn-ion binding. At the intermediate stage ($Zn_xLiV_3O_8$, $1.5 \leq x < 2$, Fig. 3h), the unit cell volume expansion is up to 16.73%, caused by the excessive zinc ion embedding. Accordingly, there is an increasement in lattice parameter by 2.07 Å and 0.14 Å in *a*-axis and *b*-axis, respectively. At the final stage (β-$Zn_yLiV_3O_8$, $2 \leq y \leq 3$, Fig. 3i), the volume expansion (7.64%) is effectively suppressed by this phase transformation. Overall, the structure/phase evolutions during the Zn^{2+}-intercalation process are interesting, which include two solid-solution reactions (from α-LiV_3O_8 to α-$Zn_{0.5}LiV_3O_8$; β-$Zn_2LiV_3O_8$ to β-$Zn_3LiV_3O_8$) separated by a two-phase process ($Zn_{0.5}LiV_3O_8$ to $Zn_2LiV_3O_8$) and a phase transformation (from α-$Zn_xLiV_3O_8$ ($x < 2$) to β-$Zn_yLiV_3O_8$ ($2 \leq y \leq 3$)).

X-ray photoelectron spectroscopic (XPS) analysis was further used to provide proof of Zn^{2+} intercalation and the valence state change of vanadium. The initial (I) and recharged stated (III) electrodes show weak signal of Zn 2p component, while the intensity of core level spectra (Zn $2p_{3/2}$: 1022.1eV; Zn $2p_{1/2}$: 1045.2 eV) increases to a very strong level at fully discharged stated (II), indicating a highly reversible insertion/desertion of Zn^{2+} in LiV_3O_8 host during discharge/charge process (Fig. 4a). For the initial electrode, three peaks located at 517.1 eV, 524.3 eV, and 530.3 eV are observed, corresponding to the binding energies of V^{5+} ($2p_{3/2}$), V^{5+} ($2p_{1/2}$), and O 1s, respectively. The signals of V^{5+} ($2p_{3/2}$) and V^{5+} ($2p_{1/2}$) are nearly replaced by the V^{3+} ($2p_{3/2}$: 515.2 eV) and V^{3+} ($2p_{1/2}$: 522.5 eV) signals at the discharged state, which indicates that all V^{5+} are converted to V^{3+} at the fully discharged state. To the contrary, the signals of V^{5+} ($2p_{3/2}$) and V^{5+} ($2p_{1/2}$) are back to the initial positions at the charged state, indicating a reversible V^{3+}/V^{5+} transformation

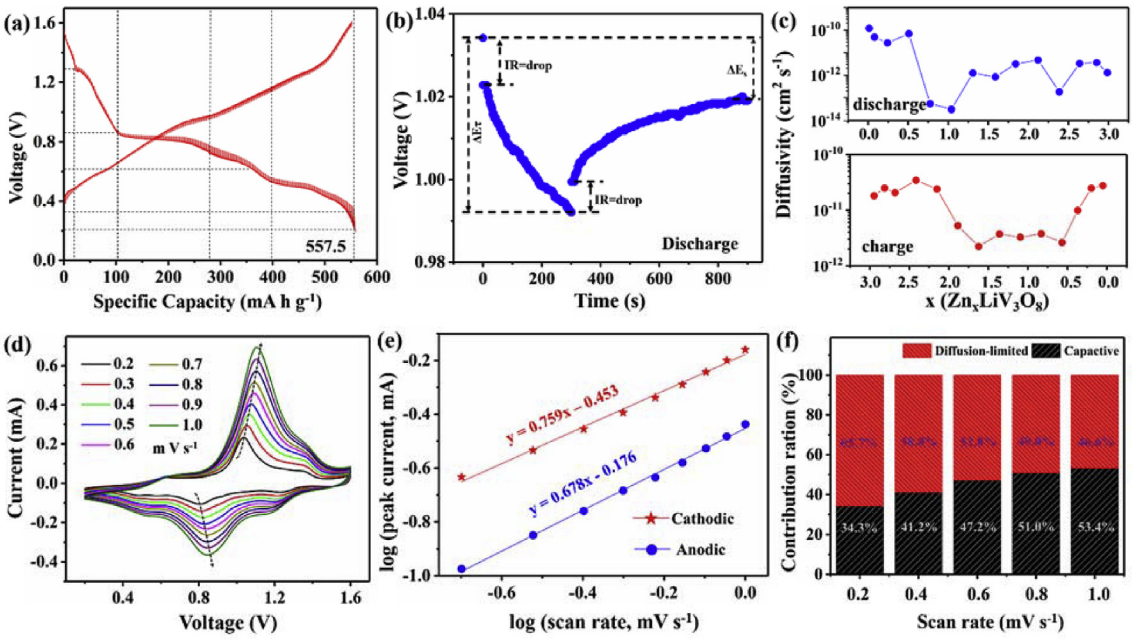

Fig. 5. (a, b) The GITT profiles at a constant current pulse of 10 mA g^{-1} for 5 min, followed by a 10 min open circuit step. (c) The diffusivity of Zn^{2+} versus the state of discharge calculated based on GITT profiles. (d) Multiple-scan rates of CV curves from 0.2 mV s^{-1} to 1.0 mV s^{-1}. (e) log(*i*) versus log(*v*) plots at specific peak currents. (f) Capacity contribution ratios at various scan rates calculated based on multiple-scan rates of CV curves.

during Zn^{2+} insertion/desertion process.

2.4. Changes in reaction kinetics

To study the reaction kinetics of Zn^{2+}-(de)intercalation process, the galvanostatic intermittent titration technique (GITT) measurements are applied (Fig. 5a–b). As shown in Fig. 5a, a very high capacity of 557.5 mA h g^{-1} at the current density of 10 mA g^{-1} is achieved at fully discharge state, indicating a reversible V^{3+}/V^{5+} double redox in LiV_3O_8 with the insertion of zinc ions. There are four plateau regions in the discharge curve and the Zn^{2+} diffusion coefficients (D_{Zn2+}) change with the discharge depth (Fig. 5c). In the first discharge plateau, the D_{Zn2+} is about 10^{-11} - 10^{-10} cm^2 s^{-1}, whereas, there are 2–3 orders of magnitude decreases of D_{Zn2+} in the second discharge plateau (~10^{-14} - 10^{-10} cm^2 s^{-1}), which is attributed to both ionic diffusion and the ions-transportation through the interphase boundary. Interestingly, the D_{Zn2+} of cathode materials increases to the magnitude of 10^{-12} cm^2 s^{-1} in the following regions, indicating a high D_{Zn2+} in this two-phase region. It's worth noting that there is a sharp decrease of D_{Zn2+} (~10^{-13} cm^2 s^{-1}) at the phase of $Zn_yLiV_3O_8$ (y ≈ 2), which should be attributed to the phase transformation between α-$Zn_xLiV_3O_8$ to β-$Zn_2LiV_3O_8$. In the final region, the D_{Zn2+} comes back to the magnitude of 10^{-12} cm^2 s^{-1}, which reflects the ionic diffusion coefficient in β-$Zn_yLiV_3O_8$ ($2 \leq y \leq 3$) phase. Similarly, the D_{Zn2+} of the cathode varies with the Zn^{2+} concentration and the phase regions during the subsequent charge process. And the D_{Zn2+} is in the magnitude of 10^{-12} - 10^{-10} cm^2 s^{-1} during the whole charging process.

The multiple-scan CV curves at the scan rates from 0.2 to 1.0 mV s^{-1} show similar shapes, and the redox peaks display gradually widening trend (Fig. 5d). The redox peaks at 0.46/0.65 fade away at high scan rates (≥0.5 mV s^{-1}), which is consistent with the charge/discharge curves that the special plateaus disappear at high rates. When increasing the scan rates from 1.0 to 10.0 mV s^{-1} (Fig. S5a), there is only one pair of reduction/oxidation peaks remained, with opposite shifting in peak potentials, and large polarization currents are generated at extremely high sweep rates (from 10.0 to 100.0 mV s^{-1}, Fig. S5b). It is assumed that the peak currents (*i*) in CV curves follow an empirical power-law regularity with the scan rate (*ν*) as below [41]:

$$i = av^b \quad (1)$$

Where a and b are adjustable parameters. The *b*-values of the cathode and anode are 0.76 and 0.68 respectively, which indicate that both solid-state diffusion-controlled intercalation and ion intercalation pseudocapacitive processes are contributed to the charge storage at the peak regions (Fig. 5e). In the further analysis based on the CV results, the currents at the peak potential regions, can be divided into two parts, including capacitive process (k_1v) and diffusion-limited process ($k_2v^{1/2}$), described below:

$$i = k_1v + k_2v^{1/2} \quad (2)$$

or

$$i / v^{1/2} = k_1v^{1/2} + k_2 \quad (3)$$

At a given voltage, the k_1-value and k_2-value characterizes the currents of capacitive and diffusion-limited process. Then the ratios of capacitive (k_1v) and diffusion-limited ($k_2v^{1/2}$) capacity contributions are obtained (based on the ratio of CV areas, Fig. S6) at varied scan rates. As shown in Fig. 5f, ~34.3% of the total capacity is contributed by capacitive properties at the scan rate of 0.2 mV s^{-1}, and nearly half of the capacity contribution comes from capacitance at 0.8 mV s^{-1}, indicating that both capacitive behavior and ion diffusion process play vital roles in the capacity contribution.

Staircase potential electrochemical impedance spectroscopy (SPEIS) measurements are performed to further understand the kinetics of Zn^{2+} diffusion and the phase transformation of the cathode closely. A potential sweep is made from $E_i = 1.6$ V to $E_f = 0.2$ V with the potential decrease of 10 mV followed by 15 min rest per step. On each step, an impedance measurement is performed for a whole frequency range from f_i = 100 kHz to $f_f = 0.01$ Hz with 71 points (Fig. S7). Generally, in the impedance profiles, an initial resistance in the high-frequency region represents the contact resistance (R_{sol}) between the Zn^{2+} and the electrolyte. The semicircle regions reflect the diffusion of Zn^{2+} in the surface layer (R_s, in the high-frequency), the charge transfer resistance (R_{ct}, in the middle-frequency region), and the diffusion of Zn^{2+} in the new phase interface (R_p) [42]. Also, the approximate straight line (in the low-frequency)

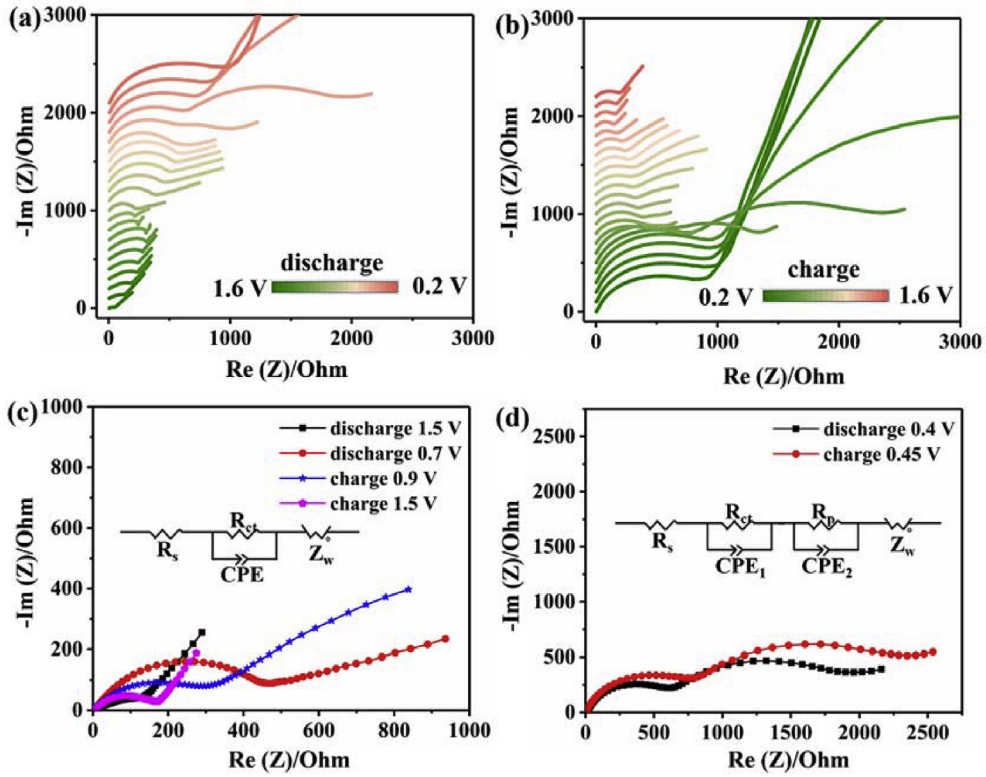

Fig. 6. The contour plots of Staircase Potential Electrochemical Impedance Spectroscopy (SPEIS). (a–b) The Nyquist impedance at selected potentials during discharge/charge process. (c–d) The fitting of Nyquist impedance at the selected potential (discharge 1.5 V, charge 1.5 V, discharge 0.7 V, charge 0.9 V; and discharge 0.4 V, charge 0.45 V).

reflects the Warburg impedance, which is related to the solid-state diffusion component. There are 140 EIS plots during the whole discharge/charge processes, and the resistance contour plots vary with the potential change (Fig. S8). In the initial discharge process (from 1.6 V to 0.85 V, green color), the impedance shows slight increase with a straight Warburg line along nearly 45°, indicating fast solid-state diffusion in this solid-solution reaction region (Fig. 6a). In the subsequent discharge process (from 0.85 V to 0.55 V, light yellow color), the impedance shows larger increase, with the straight Warburg line less than 45°, caused by the two-phase reaction mechanism. In the last stage (from 0.55 V to 0.20 V, light red color), a new semicircle appeared with large increase in impedance, which can be explained by the formation of a new phase. On the contrary, the resistances decrease during charge process, and the impedances show nearly opposite tendency to discharge as expected (Fig. 6b). The Nyquist impedance collected at selected potentials are shown in Fig. 6c, which typically represent the impedances of solid solution reaction region (discharge 1.5 V, charge 1.5 V) and two-phase reaction region (discharge 0.7 V, charge 0.9 V). Intriguingly, two semicircles are observed at the phase transformation reaction region (discharge 0.4 V, charge 0.45 V), and better fit is obtained when considering the two-step charge transfer modes (Fig. 6d). In a word, the resistance associated with the Zn^{2+} diffusion process and the phase transformation of the cathode closely, and SPEIS measurement would be an effective method to understand this process.

3. Conclusions

In conclusion, a reversible V^{3+}/V^{5+} double redox with the stepwise insertion of Zn^{2+} in LiV_3O_8 cathode was illustrated. Benefiting from this multielectron transition mechanism, the cathode delivered the highest capacity of 557.5 mA h g^{-1}, and high capacity retention of 85% over 4000 cycles, which is superior to most reported aqueous energy storage devices. Furthermore, the reaction kinetics analyses and the structural evolution characterization indicated that, although the phase transformation between α-$Zn_xLiV_3O_8$ ($x < 2$) and β-$Zn_yLiV_3O_8$ ($2 \leq y \leq 3$) lead to increased resistance and reduced kinetics of the system, it can effectively suppress the volume expansion (7.64%) of LiV_3O_8 host. Moreover, this study also shows that using V^{3+}/V^{5+} double-redox will open-up new opportunities for designing vanadium-rich cathodes for low-cost, high-performance, and environmentally friendly energy storage system.

Declaration of competing interest

The authors declare no competing interests.

CRediT authorship contribution statement

Pan He: Conceptualization, Data curation, Formal analysis, Investigation, Writing - original draft, Writing - review & editing. **Mengyu Yan:** Formal analysis, Writing - review & editing. **Xiaobin Liao:** Formal analysis, Writing - review & editing. **Yanzhu Luo:** Conceptualization, Writing - review & editing. **Liqiang Mai:** Conceptualization, Writing - review & editing. **Ce-Wen Nan:** Writing - review & editing.

Acknowledgments

This work was supported by the National Natural Science Foundation of China (51832004, 51521001), the National Key Research and Development Program of China (2016YFA0202603), the Programme of Introducing Talents of Discipline to Universities (B17034), the Yellow Crane Talent (Science & Technology) Program of Wuhan City, the Natural Science Foundation of Hubei Province (2019CFA001). We thank F. Y. Xiong and X. L. Pan for their assistance and helpful discussions in electrochemical parts.

Appendix A. Supplementary data

Supplementary data to this article can be found online at https://doi.org/10.1016/j.ensm.2020.04.005.

References

[1] M.A. Hannan, M.M. Hoque, A. Mohamed, A. Ayob, Review of energy storage systems for electric vehicle applications: issues and challenges, Renew. Sustain. Energy Rev. 69 (2017) 771–789, https://doi.org/10.1016/j.rser.2016.11.171.

[2] L. Mai, J. Sheng, L. Xu, S. Tan, J. Meng, One-dimensional hetero-nanostructures for rechargeable batteries, Acc. Chem. Res. 51 (2018) 950–959, https://doi.org/10.1021/acs.accounts.8b00031.

[3] B. Zakeri, S. Syri, Electrical energy storage systems: a comparative life cycle cost analysis, Renew. Sustain. Energy Rev. 42 (2015) 569–596, https://doi.org/10.1016/j.rser.2014.10.011.

[4] J. Muldoon, C.B. Bucur, T. Gregory, Quest for nonaqueous multivalent secondary batteries: magnesium and beyond, Chem. Rev. 114 (2014) 11683–11720, https://doi.org/10.1021/cr500049y.

[5] A. Konarov, N. Voronina, J.H. Jo, Z. Bakenov, Y.K. Sun, S.T. Myung, Present and future perspective on electrode materials for rechargeable zinc-ion batteries, ACS Energy Lett. 3 (2018) 2620–2640, https://doi.org/10.1021/acsenergylett.8b01552, 2018.

[6] P. He, Q. Chen, M. Yan, X. Xu, L. Zhou, L. Mai, C.W. Nan, Building better zinc-ion batteries: a materials perspective, EnergyChem (2019) 100022, https://doi.org/10.1016/j.enchem.2019.100022.

[7] C. Xu, B. Li, H. Du, F. Kang, Energetic zinc ion chemistry: the rechargeable zinc ion battery, Angew. Chem. Int. Ed. 51 (2012) 933–935, https://doi.org/10.1002/anie.201106307.

[8] H. Liang, Z. Cao, F. Ming, W. Zhang, D.H. Anjum, Y. Cui, H.N. Alshareef, Aqueous zinc-ion storage in MoS_2 by tuning the intercalation energy, Nano Lett. 19 (2019) 3199–3206, https://doi.org/10.1021/acs.nanolett.9b00697.

[9] P. He, M. Yan, G. Zhang, R. Sun, L. Chen, Q. An, L. Mai, Layered VS_2 nanosheet-based aqueous Zn ion battery cathode, Adv. Energy Mater. 7 (2017) 1601920, https://doi.org/10.1002/aenm.201601920.

[10] Y. Cheng, L. Luo, L. Zhong, J. Chen, B. Li, W. Wang, S.X. Mao, C. Wang, V.L. Sprenkle, G. Li, J. Liu, Highly reversible zinc-ion intercalation into chevrel phase Mo_6S_8 nanocubes and applications for advanced zinc-ion batteries, ACS Appl. Mater. Interfaces 8 (2016) 13673–13677, https://doi.org/10.1021/acsami.6b03197.

[11] L. Zhang, L. Chen, X. Zhou, Z. Liu, Towards high-voltage aqueous metal-ion batteries beyond 1.5 V: the zinc/zinc hexacyanoferrate system, Adv. Energy Mater. 5 (2015) 1400930, https://doi.org/10.1002/aenm.201400930.

[12] W. Li, K. Wang, S. Cheng, K. Jiang, A long-life aqueous Zn-ion battery based on $Na_3V_2(PO_4)_2F_3$ cathode, Energy Storage Mater. 15 (2018) 14–21, https://doi.org/10.1016/j.ensm.2018.03.003.

[13] P. Hu, Z. Zou, X. Sun, D. Wang, J. Ma, Q. Kong, D. Xiao, L. Gu, X. Zhou, J. Zhao, S. Dong, Uncovering the potential of M1-site-activated NASICON cathodes for Zn-ion batteries, Adv. Mater. (2020) 1907526, https://doi.org/10.1002/adma.201907526.

[14] G. Li, Z. Yang, Y. Jiang, C. Jin, W. Huang, X. Ding, Y. Huang, Towards polyvalent ion batteries: a zinc-ion battery based on NASICON structured $Na_3V_2(PO_4)_3$, Nano Energy 25 (2016) 211–217, https://doi.org/10.1016/j.nanoen.2016.04.051.

[15] X. Wu, Y. Xiang, Q. Peng, X. Wu, Y. Li, F. Tang, R. Song, Z. Liu, Z. He, X. Wu, Green-low-cost rechargeable aqueous zinc-ion batteries using hollow porous spinel $ZnMn_2O_4$ as the cathode material, J. Mater. Chem. 5 (2017) 17990–17997, https://doi.org/10.1039/C7TA00100B.

[16] N. Zhang, F. Cheng, Y. Liu, Q. Zhao, K. Lei, C. Chen, X. Liu, J. Chen, Cation-deficient spinel $ZnMn_2O_4$ cathode in $Zn(CF_3SO_3)_2$ electrolyte for rechargeable aqueous Zn-ion battery, J. Am. Chem. Soc. 138 (2016) 12894–12901, https://doi.org/10.1021/jacs.6b05958.

[17] M. Yan, P. He, Y. Chen, S. Wang, Q. Wei, K. Zhao, X. Xu, Q. An, Y. Shuang, Y. Shao, et al., Water-lubricated intercalation in $V_2O_5{\cdot}nH_2O$ for high-capacity and high-rate aqueous rechargeable zinc batteries, Adv. Mater. 30 (2018) 1703725, https://doi.org/10.1002/adma.201703725.

[18] F. Wang, W. Sun, Z. Shadike, E. Hu, X. Ji, T. Gao, X.Q. Yang, K. Xu, C. Wang, How water accelerates bivalent ion diffusion at the electrolyte/electrode interface, Angew. Chem. Int. Ed. 57 (2018) 11978–11981, https://doi.org/10.1002/anie.201806748.

[19] N. Zhang, F. Cheng, J. Liu, L. Wang, X. Long, X. Liu, F. Li, J. Chen, Rechargeable aqueous zinc-manganese dioxide batteries with high energy and power densities, Nat. Commun. 8 (2017) 405, https://doi.org/10.1038/s41467-017-00467-x.

[20] S.D. Han, S. Kim, D. Li, V. Petkov, H.D. Yoo, P.J. Phillips, H. Wang, J.J. Kim, K.L. More, B. Key, et al., Mechanism of Zn insertion into nanostructured δ-MnO_2: a nonaqueous rechargeable Zn metal battery, Chem. Mater. 29 (2017) 4874–4884, https://doi.org/10.1021/acs.chemmater.7b00852.

[21] H. Pan, Y. Shao, P. Yan, Y. Cheng, K.S. Han, Z. Nie, C. Wang, J. Yang, X. Li, P. Bhattacharya, et al., Reversible aqueous zinc/manganese oxide energy storage from conversion reactions, Nat. Energy 1 (2016) 16039, https://doi.org/10.1038/nenergy.2016.39.

[22] M.H. Alfaruqi, S. Islam, J. Gim, J. Song, S. Kim, D.T. Pham, J. Jo, Z. Xiu, V. Mathew, J. Kim, A high surface area tunnel-type α-MnO_2 nanorod cathode by a simple solvent-free synthesis for rechargeable aqueous zinc-ion batteries, Chem. Phys. Lett. 650 (2016) 64–68, https://doi.org/10.1016/j.cplett.2016.02.067.

[23] Y. Yin, C. Liu, S. Fan, A new type of secondary hybrid battery showing excellent performances, Nano Energy 12 (2015) 486–493, https://doi.org/10.1016/j.nanoen.2015.01.014.

[24] M.H. Alfaruqi, V. Mathew, J. Gim, S. Kim, J. Song, J.P. Baboo, S.H. Choi, J. Kim, Electrochemically induced structural transformation in a γ-MnO_2 cathode of a high capacity zinc-ion battery system, Chem. Mater. 27 (2015) 3609–3620, https://doi.org/10.1021/cm504717p.

[25] F.Y. Cheng, J. Chen, X.L. Gou, P.W. Shen, High-power alkaline Zn-MnO_2 batteries using γ-MnO_2 nanowires/nanotubes and electrolytic zinc powder, Adv. Mater. 17 (2005) 2753–2756, https://doi.org/10.1002/adma.200500663.

[26] M. Chamoun, W.R. Brant, C.W. Tai, G. Karlsson, D. Noréus, Rechargeability of aqueous sulfate Zn/MnO_2 batteries enhanced by accessible Mn^{2+} ions, Energy Storage Mater. 15 (2018) 351–360, https://doi.org/10.1016/j.ensm.2018.06.019.

[27] G. Fang, C. Zhu, M. Chen, J. Zhou, B. Tang, X. Cao, X. Zheng, A. Pan, S. Liang, Suppressing manganese dissolution in potassium manganate with rich oxygen defects engaged high-energy-density and durable aqueous zinc-ion battery, Adv. Funct. Mater. (2019) 1808375, https://doi.org/10.1002/adfm.201808375.

[28] P. He, Y. Quan, X. Xu, M. Yan, W. Yang, Q. An, L. He, L. Mai, High-performance aqueous zinc-ion battery based on layered $H_2V_3O_8$ nanowire cathode, Small 13 (2017) 1702551, https://doi.org/10.1002/smll.201702551.

[29] B. Wu, G. Zhang, M. Yan, T. Xiong, P. He, L. He, X. Xu, L. Mai, Graphene scroll-coated α-MnO_2 nanowires as high-performance cathode materials for aqueous Zn-ion battery, Small 14 (2018) 1703850, https://doi.org/10.1002/smll.201703850.

[30] C. Xia, J. Guo, P. Li, X. Zhang, H.N. Alshareef, Highly stable aqueous zinc-ion storage using a layered calcium vanadium oxide bronze cathode, Angew. Chem. Int. Ed. 57 (2018) 3943–3948, https://doi.org/10.1002/anie.201713291.

[31] P. He, G. Zhang, X. Liao, M. Yan, X. Xu, Q. An, J. Liu, L. Mai, Sodium ion stabilized vanadium oxide nanowire cathode for high-performance zinc-ion batteries, Adv. Energy Mater. 8 (2018) 1702463, https://doi.org/10.1002/aenm.201702463.

[32] D. Kundu, B.D. Adams, V. Duffort, S.H. Vajargah, L.F. Nazar, A high-capacity and long-life aqueous rechargeable zinc battery using a metal oxide intercalation cathode, Nat. Energy 1 (2016) 16119, https://doi.org/10.1038/nenergy.2016.119.

[33] W. Ren, Z. Zheng, Y. Luo, W. Chen, C. Niu, K. Zhao, M. Yan, L. Zhang, J. Meng, L. Mai, An electrospun hierarchical LiV_3O_8 nanowire-in-network for high-rate and long-life lithium batteries, J. Mater. Chem. 3 (2015) 19850–19856, https://doi.org/10.1039/C5TA04643B.

[34] Q. Zhang, A.B. Brady, C.J. Pelliccione, D.C. Bock, A.M. Bruck, J. Li, V. Sarbada, R. Hull, E.A. Stach, K.J. Takeuchi, et al., Investigation of structural evolution of $Li_{1.1}V_3O_8$ by in situ X-ray diffraction and density functional theory calculations, Chem. Mater. 29 (2017) 2364–2373, https://doi.org/10.1021/acs.chemmater.7b00096.

[35] M.H. Alfaruqi, V. Mathew, J. Song, S. Kim, S. Islam, D.T. Pham, J. Jo, S. Kim, J.P. Baboo, Z. Xiu, Electrochemical zinc intercalation in lithium vanadium oxide: a high-capacity zinc-ion battery cathode, Chem. Mater. 29 (2017) 1684–1694, https://doi.org/10.1021/acs.chemmater.6b05092.

[36] G. Yang, W. Hou, Z. Sun, Q. Yan, A novel inorganic-organic polymer electrolyte with a high conductivity: insertion of poly (ethylene) oxide into LiV_3O_8 in one step, J. Mater. Chem. 15 (2005) 1369–1374, https://doi.org/10.1039/B415041D.

[37] R. Baddour-Hadjean, A. Marzouk, J.P. Pereira-Ramos, Structural modifications of $Li_xV_2O_5$ in a composite cathode ($0 \leq x < 2$) investigated by Raman microspectrometry, J. P. J. Raman Spectrosc. 43 (2012) 153–160, https://doi.org/10.1002/jrs.2984.

[38] J. Shin, D.S. Choi, H.J. Lee, Y. Jung, J.W. Choi, Hydrated intercalation for high-performance aqueous zinc ion batteries, Adv. Energy Mater. 9 (2019) 1900083, https://doi.org/10.1002/aenm.201900083.

[39] P. Senguttuvan, S.D. Han, S. Kim, A.L. Lipson, S. Tepavcevic, T.T. Fister, I.D. Bloom, A.K. Burrell, C.S. Johnson, A high power rechargeable nonaqueous multivalent Zn/V_2O_5 battery, Adv. Energy Mater. 6 (2016) 1600826, https://doi.org/10.1002/aenm.201600826.

[40] C. Xia, J. Guo, Y. Lei, H. Liang, C. Zhao, H.N. Alshareef, Rechargeable aqueous zinc-ion battery based on porous framework zinc pyrovanadate intercalation cathode, Adv. Mater. 30 (2018) 1705580, https://doi.org/10.1002/adma.201705580.

[41] P. Simon, Y. Gogotsi, B. Dunn, Where do batteries end and supercapacitors begin? Science 343 (2014) 1210–1211, https://doi.org/10.1126/science.1249625.

[42] D. Kundu, P. Oberholzer, C. Glaros, A. Bouzid, E. Tervoort, A. Pasquarello, M. Niederberger, Organic cathode for aqueous Zn-ion batteries: taming a unique phase evolution toward stable electrochemical cycling, Chem. Mater. 30 (2018) 3874–3881, https://doi.org/10.1021/acs.chemmater.8b01317.